Northumbria Research Link

Northumbria University
NEWCASTLE

University Library

Discrete Self-Imaging in Small-Core Optical Fiber Interferometers

Xiaokang Lian, Qiang Wu, Gerald Farrell, Changyu Shen, Youqiao Ma, and Yuliya Semenova.

Abstract—**Multiple cladding modes can exist in a small-core optical fiber unaccompanied by core modes, yet this fact has not been sufficiently explored in literature to date. In this article, we study the self-imaging of cladding modes in small core optical fiber interferometers. Our analytical and numerical simulations and experiments show that unlike the self-imaging of core modes, self-imaging of cladding modes only appears at a set of discrete positions along the interferometer axis with an equal spacing corresponding to some discrete values of fiber core radius. This is the first observation of the discrete self-imaging effect in multimode waveguides. More strikingly, the self-imaging period of cladding modes grows exponentially with fiber core radius, unlike the quadratic relationship in the case of core modes. The findings bring new insights to the mode propagation in an optical fiber with a core at micro/nanoscale, which may open new avenues for exploring multimode fiber technologies in both linear and nonlinear optics.**

Index Terms—**Optical fiber cladding, Optical fiber devices, Optical fiber interference, Self-focusing, Talbot and self-imaging effect.**

I. Introduction

MULTIMODE FIBERS (MMFs) have acquired significant popularity in areas such as telecommunications [1], [2], microscopic imaging [3], optical manipulation [4], [5], fiber lasers and amplifiers [6], [7]. Moreover, MMFs provide new degrees of freedom and opportunities in linear and the non-linear optics, which are not possible to realize with single-mode fibers (SMFs) [8]-[10]. Most of the research relating to single-core step-index MMFs [3], [4], no-core fibers (NCFs)

X. Lian, G. Farrell, and Y. Semenova are with the Photonics Research Center, Technological University Dublin, Dublin, Ireland (e-mail: xiaokang.lian@mydit.ie; gerald.farrell@dit.ie; yuliya.semenova@dit.ie).

Q. Wu is with the Department of Mathematics, Physics, and Electrical Engineering, Northumbria University, Newcastle upon Tyne NE1 8ST, U.K. (e-mail: qiang.wu@northumbria.ac.uk).

C. Shen is with the Institute of Optoelectronic Technology, China Jiliang University, Hangzhou 310018, China (e-mail: shenchangyu@cjlu.edu.cn).

Y. Ma is with the Department of Electrical and Computer Engineering, Dalhousie University, Halifax B3H 4R2, Canada (e-mail: mayouqiao188@hotmail.com).

[5], graded-index fibers [2], [10] and multicore fibers [1] has focused on studies of the core modes, which propagate mainly in the core region. In fact, the cladding region of an optical fiber can also act as a waveguide and can support multiple cladding modes, which can be excited in a standard SMF by a fiber Bragg grating (FBGs) or a long-period grating [11]. Cladding modes are useful in many applications such as sensing and integrated optical devices [12], [13], for example in sensing, cladding modes can interact much more readily with the surrounding environment. Mathematically the core modes and the cladding modes are characterized by different functions arising from different solutions of the Bessel equation [11], [14], J_m and K_m for the core modes and functions J_m, Y_m and K_m for the cladding modes. Therefore, the cladding modes may have some distinct characteristics compared to core modes. Unfortunately, cladding modes excited by FBGs usually coexist alongside with the core modes, making it impossible for the cladding modes to be studied independently from the core modes [11], [15], [16]. It was common belief that there are no principal differences between the cladding modes and the core modes in optical fiber, except that they have different transverse intensity distributions [11].

The modal distribution in a step-index optical fiber depends on the value of the *V*-parameter, defined as:

$$V = \frac{2\pi r_{co}}{\lambda} \sqrt{n_{co}^2 - n_{cl}^2} \tag{1}$$

where r_{co}, n_{co} and n_{cl} are the core radius and refractive indices of the fiber core and cladding respectively, and λ is the light wavelength. When $V < 1$, the core modes are cancelled out leaving only the cladding modes, and thus create a unique opportunity for investigation of pure cladding modes [17]-[19]. To satisfy the condition $V < 1$, the r_{co} should reach micro/nanoscale, which occurs in a small-core fiber (SCF). In an SCF, a very small core surrounded by a much larger silica cladding is analogous to optical microfibers and nanofibers which in effect possess an air cladding. Microfibers and nanofibers can offer numerous favorable properties such as strong evanescent fields, tight light confinement and large and manageable waveguide dispersion for manipulating light at micro/nanoscale, which has shown to be advantageous in a wide range of applications such as optical communication, sensors, laser and nonlinear optics [20]-[22]. An SCF with a core at micro/nanoscale may have different properties than that of the commonly used SMF and MMF. However it has not been sufficiently explored in literature to date [23], [24].

The fundamental mode in both NCF and SMF is a core-type mode. However in an SCF the fundamental mode is a cladding-type mode because the core radius in the SCF is too small to support any core modes. Increasing the core radius of

the SCF will lead to transfer of the fundamental mode from a cladding-type to a core-type as the cut-off condition is met. The mode transition phenomenon is usually relevant to many techniques such as single-mode operation, mode selective excitation and evanescent coupling, which are important to the design of fiber lasers, sensors, devices for optical networks [25]-[31].

Self-imaging is a property of multimode waveguides by which an input field profile is reproduced as single or multiple images at periodic lengths along the propagation direction of the waveguide [32]. The self-imaging effect is widely employed in design of multimode waveguide devices such as power splitters/combiners, Mach-Zehnder switches/modulators, high power laser diodes and semiconductor optical amplifiers [32]-[40]. Self-imaging is also important for studies of the exciting physical phenomena recently found in multimode nonlinear fiber optics such as the geometric parameter instability [41], spatial beam self-cleaning [10], multimode solitons and ultrabroadband dispersive radiation [42]. Self-imaging in multimode waveguides is closely related to the propagation constants of the guided modes. Based on the approximate expression for the propagation constants of the core modes, the self-imaging period (L_Z) for an optical fiber interferometer (OFI) utilizing a fiber hetero-structure SMF-MMF-SMF (SMS) is a quadratic function of the r_{co} of the MMF section, presented by W. S. Mohammed *et al.* in [33] as:

$$L_Z = \frac{8 n_{co} k_0 r_{co}^2}{\pi} \qquad (2)$$

where $k_0 = 2\pi/\lambda$ is the wavenumber. This quadratic relationship is also suitable in the case of the OFI consisting of the fiber combination SMF-NCF-SMF (SNCS) [34]-[37]. Studies of self-imaging in a small-core optical fiber interferometer SMF-SCF-SMF (SSCS) may be an effective way to investigate the properties of cladding modes.

In this article, we present a comparative study of the self-imaging of core modes and cladding modes in SSCS, SNCS and SMS structures. The modal characteristics of core modes and cladding modes are analyzed. The discrete nature and exponential growth behavior of the self-imaging in SSCS are predicted independently by both analytical and numerical simulations and verified by spectral measurements. The discrete nature is analyzed based on the constructive interference of adjacent radial modes. The implications of the results for linear and nonlinear multimode fiber optics are discussed.

II. METHODS

Fig. 1 shows three different types of OFIs: SNCS (a), SSCS (b) and SMS (c). In an OFI, the fundamental mode of the input SMF is at first coupled into the guided modes in the middle fiber section and after propagating through the middle fiber section light is then re-coupled into the output SMF. The guided modes in the middle fiber section can be represented as radial LP_{0n} modes for the on-axis excitation, as shown in Fig. 1(d). Due to the difference in the propagation constants (phase) of LP_{0n}, constructive or destructive modal interferences occur along the middle fiber section. At the periodic self-imaging positions, the input field is replicated along the middle fiber section in both amplitude and phase. The structural and material features of the middle fiber section

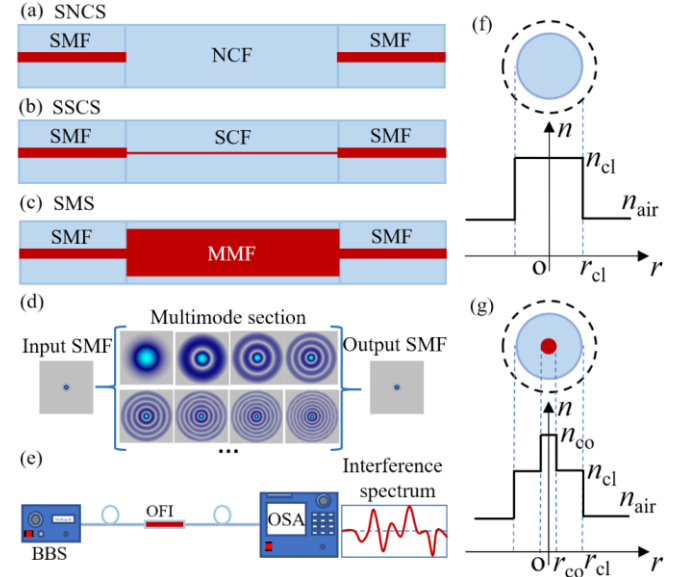can be determined by measuring the interference spectrum

Fig. 1. (a), (b) and (c) are respectively the SMF-NCF-SMF (SNCS), SMF-SCF-SMF (SSCS) and SMF-MMF-SMF (SMS) optical fiber interferometers (OFIs). (d) The transverse intensity profile of fundamental modes in the input and output SMFs, and partial LP_{0n} modes in middle fiber section. (e) Experimental setup for the measurement of the multimode interference spectra. (f) and (g) are respectively the refractive index variation along a cross section radius of an optical fiber placed in the air without (NCF) and with (SMF, SCF and MMF) a fiber core.

using an experimental setup shown in Fig. 1(e).

The cross-sectional views of the NCF are shown in Fig. 1(f) while a general model for the SMF, SCF and MMF is shown in Fig. 1(g), where we have assumed that the fibers are placed in the air. In the simulations, the r_{co} of the middle fiber section of the OFI is the only variable parameter, covering the entire radial range from 0 to 62.5 μm. The other parameters for the middle fiber section are: $r_{cl} = 62.5$ μm, $n_{co} = 1.451$ and $n_{cl} = 1.445$ ($\lambda = 1550$ nm). The parameters of the input/output SMF are $r_{co} = 4.15$ μm, $r_{cl} = 62.5$ μm, $n_{co} = 1.4504$ and $n_{cl} = 1.4447$. The refractive index of the surrounding medium (air) is $n_{air} = 1$. It should be noted that both the fibers with r_{co} equal to 0 μm and 62.5 μm are NCFs (bare fibers, which in effect possess an air cladding). In this work, the refractive index of NCF with $r_{co} = 0$ μm is equal to 1.445 (same as the n_{cl} of SCF, as shown in Fig.1(f)), while the one with $r_{co} = 62.5$ μm is equal to 1.451 (the n_{co} of SCF).

The simulations were carried out by both an analytical and a numerical method, including the effective refractive index (n_{eff}), the transverse intensity profile (TIP), the longitudinal intensity distribution (LID), the on-axis intensity, and the transmission spectra. In the analytical method, a guided-mode propagation analysis (MPA) was employed, with the field functions and the eigenvalue equations for three-layer step-index optical fibers (shown in Fig.1(g)). In the numerical method, a commercial software package BeamPROP (Rsoft, Pasadena, CA, USA) based on a 3-dimensional finite difference beam propagating method (FD-BPM) was used. All the simulations were performed in the scalar mode, under the assumption that the linear polarization (LP) approximation is valid for the fiber due to a relatively small difference between the core and cladding n_{co} (1.451) and n_{cl}

(1.445). The LP approximation is also suitable for the NCF (SNCS) due to the mode fields far from cutoff [35], although the difference between n_{cl} and n_{air} is relatively large. In the BPM simulation of the n_{eff}, TIP, LID and on-axis intensity, the <u>mesh</u> size is 0.05 µm along the X and Y directions and 1 µm along the Z direction. In the BPM simulation of transmission spectra, the <u>mesh</u> size is 0.2 µm along the X and Y direction and 4 µm along the Z direction.

In the experiments, the broadband light source (Thorlabs S5FC1005s, 1030 nm-1660 nm) and the optical spectrum analyser (OSA, Agilent 86142B) were used. The middle fiber section in the OFIs were <u>cleaved</u> and measured manually, the measurement error of the length was controlled to within 0.03 mm. The OFIs were fabricated by automated fusion splicing.

III. RESULTS

A. The LP$_{0n}$ modes in OFIs

As mentioned in the previous section, the guided modes in the middle fiber section of OFIs can be represented as radial modes LP$_{0n}$ for the on-axis excitation. Since both the cladding modes and core modes are studied in this work, the field profiles of LP$_{0n}$ in a three-layer step-index optical fiber are used and written as [43], [19]:

$$E_{0n}(r) = \begin{cases} A_0 J_0\left(u\dfrac{r}{r_{co}}\right), & r \le r_{co} \\ A_1 J_0\left(u'\dfrac{r}{r_{cl}}\right) + A_2 Y_0\left(u'\dfrac{r}{r_{cl}}\right), & \\ & r_{co} \le r \le r_{cl} \\ A_3 K_0\left(v\dfrac{r}{r_{cl}}\right), & r \ge r_{cl} \end{cases} \text{ if } n_{eff} < n_{cl}$$

(3)

And as

$$E_{0n}(r) = \begin{cases} A'_0 J_0\left(u\dfrac{r}{r_{co}}\right), & r \le r_{co} \\ A'_1 I_0\left(v'\dfrac{r}{r_{cl}}\right) + A'_2 K_0\left(v'\dfrac{r}{r_{cl}}\right), & \\ & r_{co} \le r \le r_{cl} \\ A'_3 K_0\left(v\dfrac{r}{r_{cl}}\right), & r \ge r_{cl} \end{cases} \text{ if } n_{eff} > n_{cl}$$

(4)

where J_0, Y_0, I_0 and K_0 are zero-order usual Bessel and modified Bessel functions, A_0, A'_0, are the normalization coefficients and u, u', v, v', A_1, A'_1, A_2, A'_2, A_3 and A'_3 are defined as follows:

$$u = a[k_0^2 n_{co}^2 - (n_{eff}k_0)^2]^{1/2} \tag{5-1}$$

$$u' = b[k_0^2 n_{cl}^2 - (n_{eff}k_0)^2]^{1/2} \tag{5-2}$$

$$v' = b[(n_{eff}k_0)^2 - k_0^2 n_{cl}^2]^{1/2} \tag{5-3}$$

$$v = b[(n_{eff}k_0)^2 - k_0^2 n_{air}^2]^{1/2} . \tag{5-4}$$

$$A_1 = \frac{\pi A_0}{2}[uJ_1(u)Y_0(u'c) - u'cJ_0(u)Y_1(u'c)] \tag{6-1}$$

$$A_2 = \frac{\pi A_0}{2}[u'cJ_1(u'c)J_0(u) - uJ_1(u)J_0(u'c)] \tag{6-2}$$

$$A_3 = \frac{1}{K_0(v)}[A_1 J_0(u') + A_2 Y_0(u')] \tag{6-3}$$

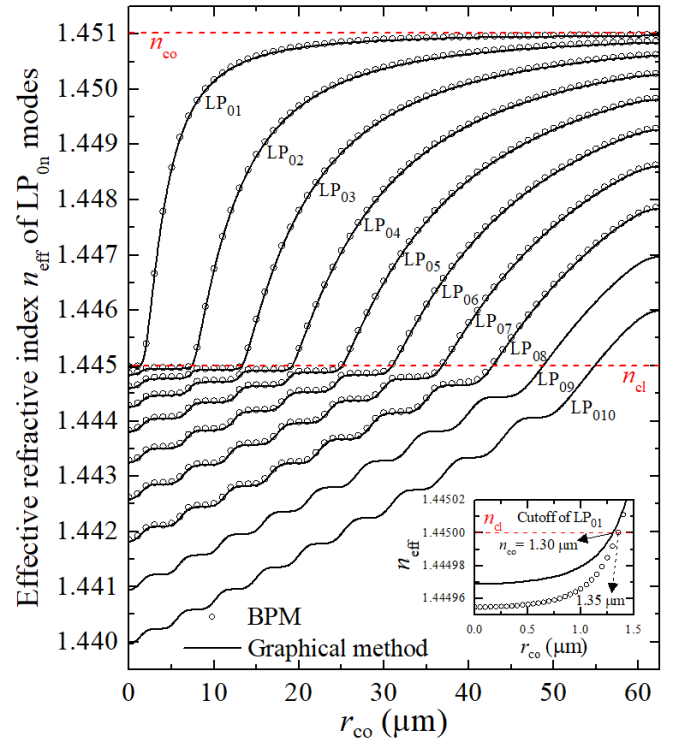$$A'_1 = A'_0[v'cJ_0(u)K_1(v'c) - uJ_1(u)K_0(v'c)] \tag{7-1}$$

Fig. 2. The effective refractive index of the modes LP$_{0n}$ as a function of fiber core radius. The solid curves are results calculated by the graphical method, while the scattered circles are results calculated by the BPM. The inset shows that the cutoff of the LP$_{01}$ mode changing from cladding-type to core-type is r_{co} = 1.30 µm (graphical method) and r_{co} = 1.35 µm (BPM).

$$A'_2 = A'_0[v'cJ_0(u)I_1(v'c) + uJ_1(u)I_0(v'c)] \tag{7-2}$$

$$A'_3 = \frac{1}{K_0(v)}[A'_1 I_0(v') + A'_2 K_0(v')] \tag{7-3}$$

The n_{eff}(LP$_{0n}$) is the solution of the eigenvalue equations as below [43]:

$$\frac{[\hat{J}_0(u)-\hat{Y}_0(u'c)][\hat{K}_0(v)-\hat{J}_0(u')]}{[\hat{J}_0(u)-\hat{J}_0(u'c)][\hat{K}_0(v)-\hat{Y}_0(u')]} = \frac{J_1(u'c)Y_1(u')}{J_1(u')Y_1(u'c)} \quad \text{if } n_{eff} < n_{cl}$$

(8)

and

$$\frac{[\hat{J}_0(u)-\hat{K}_0(v'c)][\hat{K}_0(v)+\hat{I}_0(v')]}{[\hat{J}_0(u)+\hat{I}_0(v'c)][\hat{K}_0(v)-\hat{K}_0(v')]} = \frac{I_1(v'c)K_1(v')}{I_1(v')K_1(v'c)} \quad \text{if } n_{eff} > n_{cl}$$

(9)

where

$$\hat{F}_0(x) = \frac{F_0(x)}{xF_1(x)} \tag{10}$$

(F representing the Bessel functions J, Y, I, or K) and

$$c = \frac{r_{co}}{r_{cl}} \tag{11}$$

<u>Equations</u> (8) and (9) were solved by the graphical method and the results of the n_{eff} for the first 10 LP$_{0n}$ modes are shown as a function of r_{co} in Fig. 2 (solid curves). The n_{eff}(LP$_{0n}$) (n = 1, 2, …, 8) calculated by BPM are also shown in Fig. 2 (scattered circles). Due to the setting limits of mode number in the commercial software, only 8 modes were found with BPM. Clearly, the results from the analytical method and the BPM are consistent with each other.

Fig. 2 is divided into two parts by the red dash horizontal lines located at n_{co} and n_{cl}. The region with $n_{cl} < n_{eff} < n_{co}$ corresponds to the fiber core modes while the region with $n_{eff} < n_{cl}$ ($r_{co} \ne 0$ µm) is corresponding to the fiber cladding modes. All the modes in NCFs with $r_{co} = 0$ µm or $r_{co} = 62.5$ µm are
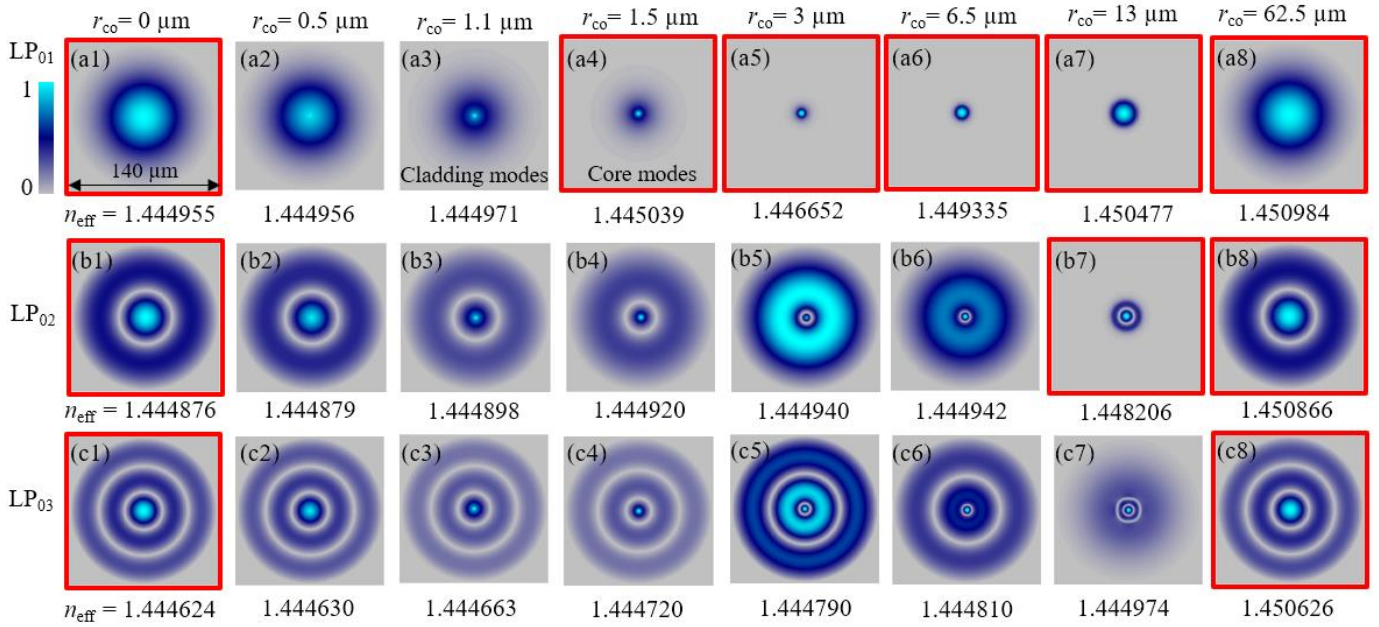
Fig. 3. The field distribution of the modes LP$_{01}$ (a1-a8), LP$_{02}$ (b1-b8), and LP$_{03}$ (a1-c8) for several different r_{co} as indicated, calculated by the BPM. The modes a1, b1 c1, a8, b8 and c8 in the no-core fibers are core-type modes; the a4-a7, b7 are also core-type modes for $n_{eff} > 1.445$; the rest are cladding-type modes with $n_{eff} < 1.445$. (The core-type modes are indicated by the red frames)

classified as core-type modes, since no guided mode can exist in an infinite air cladding region. The difference in their values of n_{eff} is due to the different refractive indices of the bare fiber, as mentioned in the section II. When a micro/nano-core exists in the central region of the fiber, the fiber is SCF. The SCF studied in this work has a core radius smaller than the cut-off radius of LP$_{01}$, where all the guided modes LP$_{0n}$ are cladding-type mode due to $n_{eff} < n_{cl}$. As the r_{co} increases, the LP$_{0n}$ modes change from cladding-type modes to core-type modes following the order from low to high. The behavior of curves in the region $n_{eff} < n_{cl}$ shows a feature of the modal reorganization (when one cladding mode moves into the core region, the next mode will take its original position), which is similar to the modal re-organization in overlay-coated long-period gratings and SMS [25], [26].

The cutoff of LP$_{01}$ calculated by the BPM is found at about $r_{co} = 1.35$ μm as seen in the inset graph of Fig. 2. Which is slightly larger than the result ($r_{co} = 1.30$ μm) calculated by the graphical method. The difference between the BPM results and the results from the graphical method may be attributed to the mesh size used in the former method. The mesh size in the numerical simulation may affect the accuracy of the results. In our work, we have tried several different mesh sizes and finally chose the best one by balancing simulation time with accuracy. It should be noted that the mesh size in the simulation here is the same as that in the simulation of on-axis intensity, from which the self-imaging period is decided as discussed later. The V-parameter is smaller than 0.7214 for the optical fibers with $r_{co} < 1.35$ μm.

Fig. 3 shows the field distribution of the modes LP$_{01}$, LP$_{02}$, and LP$_{03}$ for several core radii, calculated by the BPM. The core-type modes are indicated by red frames, while the rest are cladding-type modes. The field profiles in Fig. 3 show the characteristics, as demonstrated in [27], that the energy of core modes is concentrated mainly inside the fiber core while the part distributed inside the cladding region decreases

exponentially with increasing distance from the core boundary. The energy in the cladding modes can extend throughout the core and cladding regions. All the modes in NCF indicated by $r_{co} = 0$ μm are core-type modes as shown in Figs. 3(a1), 3(b1) and 3(c1), where the energy is extended throughout the whole fiber cross section. As the r_{co} increases from 0 to 1.1 μm, the n_{eff} of modes LP$_{01}$, LP$_{02}$ and LP$_{03}$ increase while their central intensity (bright circle) area reduces. The LP$_{01}$ becomes a core-type mode beyond the value of r_{co} around 1.3 μm. As shown in Figs. 3(a4)-3(a7), the energy of LP$_{01}$ is concentrated mainly inside the fiber core. The LP$_{02}$ changes into a core-type mode as soon as the core radius becomes large enough. Fig. 3(b7) shows the field distribution of core-type LP$_{02}$ mode with $r_{co} = 13$ μm, where the energy distribution area including both the central circle and the outer ring is concentrated mainly inside the fiber core. When r_{co} grows up to 62.5 μm, the fiber becomes an NCF again, for which all the modes belong to core-type modes similar to NCF with $r_{co} = 0$ μm, shown in Fig. 3(a8), 3(b8) and 3(c8).

B. The self-imaging periods

The field of the fundamental mode of the input SMF is denoted by $E_s(r)$. The excited optical field in the middle fiber section of OFIs can be represented by the superposition of E_{0n}(LP$_{0n}$) and shown as:

$$E_s(r, 0) = \sum_{n=1}^{N} c_n E_{0n}(r) \quad (12)$$

where E_{0n} is expressed by (3) and (4), and c_n is the coupling coefficient between the fundamental mode of SMF and the LP$_{0n}$ in the middle fiber section, which is calculated as follows:

$$c_n = \sqrt{\eta_n} \quad (13)$$

$$\eta_n = \frac{\left| \int_0^\infty E_s(r) E_{0n}(r) r dr \right|^2}{\int_0^\infty |E_s(r)|^2 r dr \int_0^\infty |E_{0n}(r)|^2 r dr} \quad (14)$$
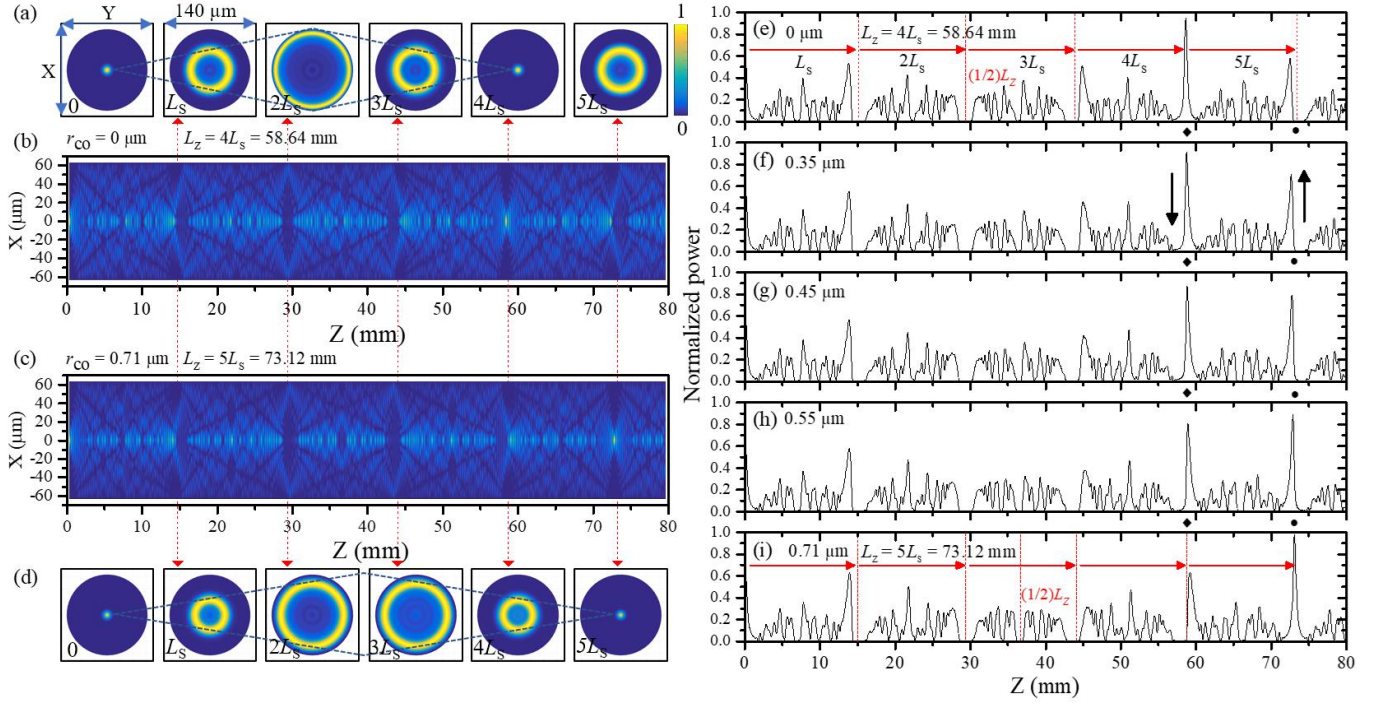
Fig. 4. Analytical results: (a), (b) and (e) are the transverse intensity profile (TIP), the longitudinal intensity distribution (LID) and the on-axis intensity along the propagation distance inside the NCF of SNCS (r_{co} =0 µm). (f), (g) and (h) are the on-axis intensities inside the SCF of SSCS with the r_{co} equal to 0.35 µm, 0.45 µm and 0.55 µm. (d), (c) and (i) are the simulated TIPs, the LIDs and the on-axis intensities inside the SCF of SSCS with the r_{co} equal to 0.71 µm.

The field propagating along the middle fiber section can be written as follows:

$$E(r,z) = \sum_{n=1}^{N} c_n E_{0n}(r) \exp(j\beta_{0n}z) \qquad (15)$$

where $\beta_{0n} = k_0 n_{eff}(LP_{0n})$ is the propagation constant of LP_{0n}. The starting point along the Z-axis is at the splice between the input SMF and the middle fiber section. The on-axis intensity (normalized to the input power) along the propagation distance 'Z' inside the middle fiber section can be calculated as follows:

$$I(z) = \frac{\left|\int_0^\infty E_S(r,0)E(r,z)r dr\right|^2}{\int_0^\infty |E_S(r,0)|^2 r dr \int_0^\infty |E(r,z)|^2 r dr}. \qquad (16)$$

Figs. 4(a), (b) and (e) show respectively the TIP of the optical field in XY plane, the LID in XZ plane and the on-axis intensity along the propagation distance in the middle fiber section (NCF) of the SNCS. The light field is focused at the center of the TIP at the position Z = $4L_S$ (58.64 mm), coinciding with the profile of the input field (the fundamental mode of the input SMF) at the position Z = 0, as shown in Fig. 4(a). The on-axis intensity peak at the position Z = $4L_S$ (indicated by the black diamond symbols in Fig. 4(e)) is equal to 0.98 of the input power, which is clearly larger than those of the neighboring maxima, corresponding to bright points at the same position in Figs. 4(a) and 4(b). It should be noted that achieving 100% perfect self-imaging (the normalized power is equal to 1) is impossible due to phase mismatches [36]. These features are consistent with the results in [34], [35], indicating that an explicit self-imaging of the input field is formed and the self-imaging period L_Z for SNCS is equal to 58.64 mm. The result of L_Z = 58.64 mm is in reasonable agreement with the result of L_Z = 58.24 mm calculated by (2).

One self-imaging period of the SNCS can be divided into four segments with equal lengths of L_S (= $L_Z/4$). Unlike the

light field focused at the center of the TIP (point-like image) at the self-imaging position (Z = $4L_Z$) shown in Fig. 4(a), light fields at positions Z = $1L_S$, $2L_S$ and $3L_S$ are mainly focused within a ring area with a certain width, according to the results of lateral field profiles calculated analytically in [34].

Similarly, it can be deduced from Figs. 4(c), 4(d) and 4(i) that the other explicit self-imaging is formed at Z = $5L_S$ (73.12 mm) in the case of SSCS with r_{co} = 0.71 µm. For the intermediate transition state where 0 µm < r_{co} < 0.71 µm as shown in Figs. 4(f)-4(h), no self-imaging point exists. The decision was based on the following considerations. As the r_{co} increases above 0 µm, the intensity of the peak at the position Z = $4L_S$ (indicated by the black diamond symbols) decreases monotonically while the value of the peak at Z = $5L_S$ (indicated by the black dot symbols) increases monotonically, as shown in Figs. 4(e)-4(i). When the critical point (r_{co} = 0.71 µm) is reached, the intensity value at Z = $5L_S$ achieves its maximum while the value at Z = $4L_S$ decreases as shown in Fig. 4(i). For clarity, the intensities of the peak around the positions Z = $4L_S$ and Z = $5L_S$ as shown in Figs. 4(e)-4(i) are respectively redrawn in Figs. 5(a) and 5(b) as a function of r_{co}. The r_{co} of the top position in Fig. 5(b) is corresponding to the self-imaging radius r_{co} = 0.71 µm. Based on the monotonic and deterministic evolution of the on-axis intensity, it can be deduced that the explicit self-imaging is only formed at a critical core radius such as r_{co} = 0.71 µm. In other word, the explicit self-imaging in the SSCS only occurs at some discrete values of the core radius of the SCF.

As the r_{co} increases, the L_Z will increase. Another set of values for r_{co} allowing one to achieve explicit self-imaging are shown in Fig. 6, where the L_Z grows up to $6L_S$, $7L_S$, $8L_S$, $9L_S$ and $10L_S$ for r_{co} equal to 0.91 µm (Fig. 6(a)), 1.02 µm (Fig. 6(b)), 1.11 µm (Fig. 6(c)), 1.18 µm (Fig. 6(d)) and 1.23 µm
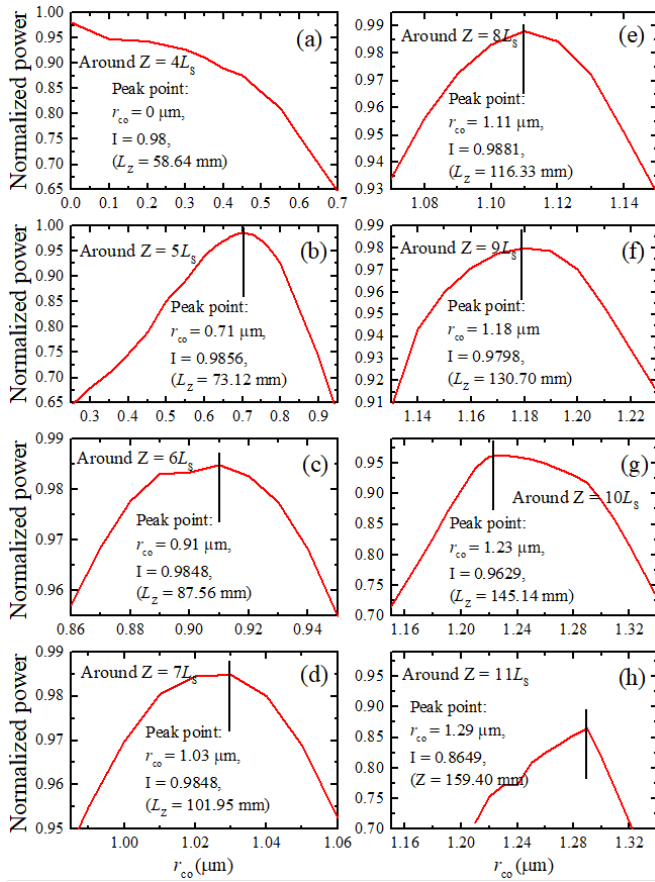
Fig. 5. Analytical results: (a)-(h) shows respectively the intensity 'I' of peak around the positions Z = nL$_S$, n = 4, 5, …,11 as a function of r_{co}. The peak points in Figs. 5(a)-5(g) correspond to the self-imaging points as shown in Figs. 4 (e), 4(i) and 6(a)-6(e).

(Fig. 6(e)). These self-imaging points respectively correspond to the peak points for the curves shown in Figs. 5(c), 5(d), 5(e), 5(f) and 5(g). Beyond the value of $r_{co} = 1.23$ µm, the intensity of the peak around Z = 10L$_S$ decreases as the r_{co} increases, as shown in Fig. 5(g). The intensity of the peak around the position Z = 11L$_S$ shown in Fig.5(h) is always smaller than the value at position Z = 10L$_S$ in Fig. 5(g). These features indicate that there is no explicit self-imaging at the position Z = 11L$_S$.

The discrete self-imaging phenomenon was also confirmed by the BPM. The results are shown in Fig. 7, where the L_Z grows as 4L$_S$, 5L$_S$, 6L$_S$, 7L$_S$, 8L$_S$, 9L$_S$ and up to 10L$_S$ for r_{co} equal to 0 µm (SNCS, Fig. 7(a)), 0.73 µm (Fig. 7(b)), 0.92 µm (Fig. 7(c)), 1.04 µm (Fig. 7(d)), 1.12 µm (Fig. 7(e)), 1.20 µm (Fig. 7(f)) and 1.27 µm (Fig. 7(g)). Both the analytical and the BPM results indicate that the self-imaging period of the SSCS is discrete and is closely related to that of the SNCS ($r_{co} = 0$ µm): L_Z(SSCS) = (1+q/4)L_Z(SNCS) = (4+q)L_S, where "q" is a positive integer and $1 \leq q \leq 6$.

The values of the discrete self-imaging periods calculated by both the analytical method and BPM were extracted and fitted with an exponential function, as shown in Fig. 8. The fitting function can be written as:

$$L_Z = L_{Z0} + B_1 \exp(\frac{r_{co}}{t_1}) \qquad (17)$$

For the case of analytical method, the R-squared value is 0.99976; $B_1 = 1.53093 \pm 0.10829$; $t_1 = 0.30396 \pm 0.00511$;
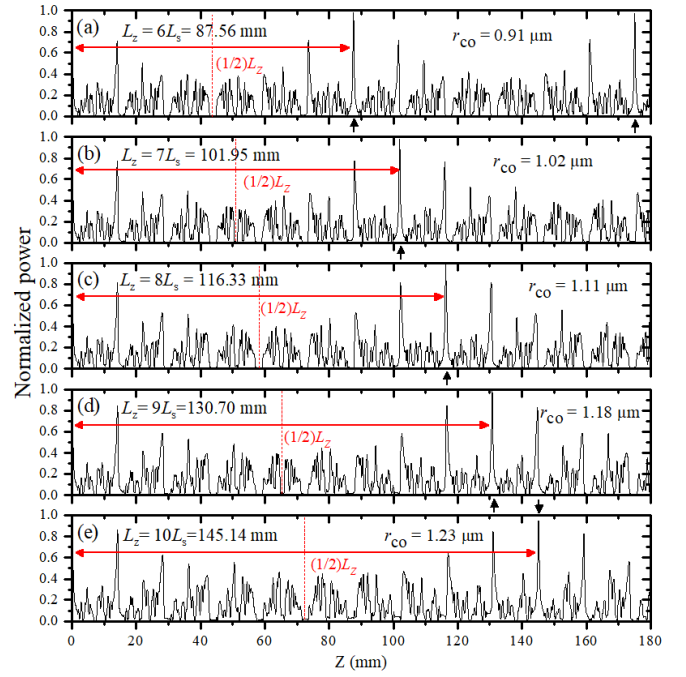
Fig. 6. Analytical results: the on-axis intensities inside the SCF of SSCS with the r_{co} equal to (a) 0.91 µm, (b) 1.02 µm, (c) 1.11 µm, (d) 1.18 µm and (e) 1.23 µm.
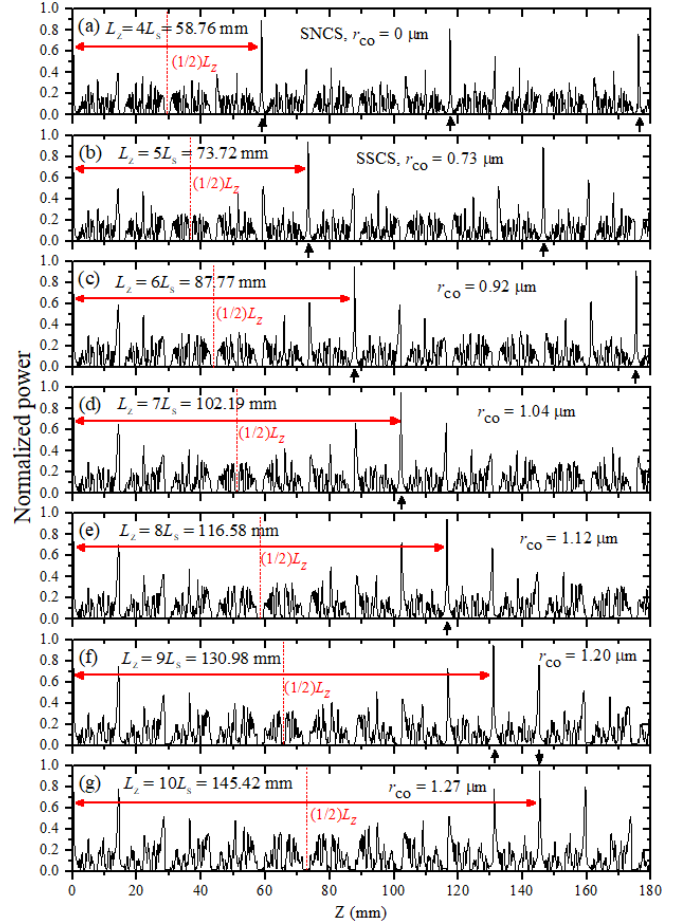

Fig. 7. BPM results: the on-axis intensities inside (a) the NCF of SNCS, the SCF of SSCS with the r_{co} equal to (b) 0.73 µm, (c) 0.92 µm, (d) 1.04 µm, (e) 1.12 µm, (f) 1.20 µm and (g) 1.27 µm.

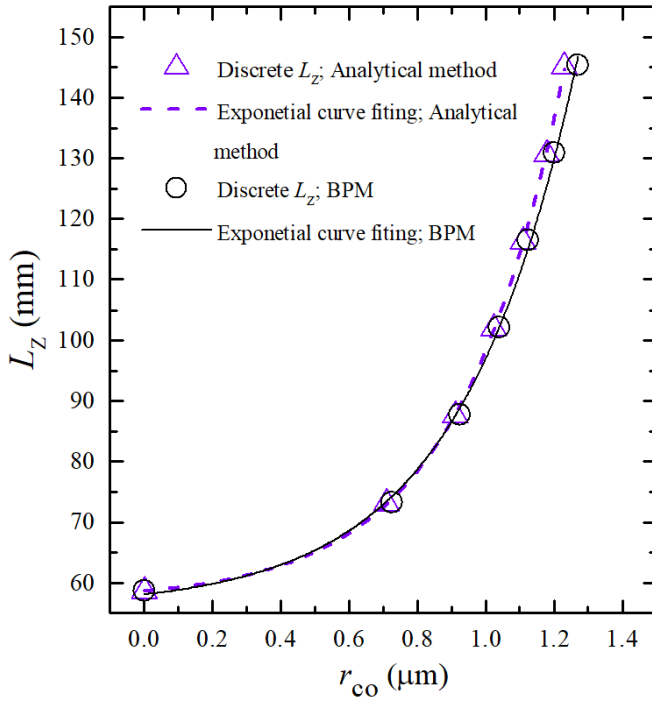$L_{Z0}= 57.15441 \pm 0.54124$ mm. For the case using the BPM, the R-squared value is 0.99804; $B_1 = 2.17781 \pm 0.40074$;

Fig. 8. The discrete and exponential growth of the self-imaging period L_Z for the SNCS ($r_{co} = 0$ μm) and the SSCS versus r_{co}, calculated both by the analytical method and BPM.

Fig. 9. (a) The values of L_{Zn} calculated by (19): $L_{Zn} = (4n-3)L_n$ with the $n_{eff}(LP_{0n})$ determined from the graphical results in Fig.2. The main graph of (b) shows the parts extracted from (a), related to the pure core modes. The inset of (b) shows the part extracted from (a), related to the cladding modes of SCF with 0 μm < r_{co} < 1.3 μm and the core modes of NCF with $r_{co} = 0$ μm.

$t_1 = 0.3404 \pm 0.01606$; $L_{Z0} = 55.92114 \pm 1.62183$ mm. In both cases, r_{co} is a set of discrete values. The L_{Z0} in both cases is close to the L_Z of SNCS ($r_{co} = 0$ μm). The results calculated independently by two different methods are highly consistent, although there is a slight difference between the results at the relatively large r_{co}. The difference may be due to the mesh size, which affects the accuracy of the numerical results as discussed in the part A.

C. Exploration of the discrete characteristics

The light field in the middle fiber section of OFI is a superposition of all the guided modes LP_{0n}. At a self-imaging position, a constructive interference will occur among all of them. Surprisingly, the self-imaging period L_Z in SMS is closely related to the constructive interference length L_n of two adjacent guided modes [33]. L_n is calculated for two adjacent modes (LP_{0n-1} and LP_{0n}) when their phase difference equals 2π:

$$L_n = \frac{2\pi}{(\beta_{n-1} - \beta_n)} = \frac{\lambda}{[n_{eff}(LP_{0n-1}) - n_{eff}(LP_{0n})]}, n = 2, 3, \ldots \ (18)$$

These two adjacent guided modes will also experience constructive interference at the position qL_n ($q = 1, 2, \ldots$ is an integer number). It was stated that the L_Z is an integer multiple of L_p: $L_Z = (4p-3)L_p$, where the modal number p is related to the mode LP_{0p} holding the highest coupling efficiency [33]. However, the L_Z may be not restricted to the mode with the highest coupling efficiency. Using L_n of any two adjacent modes, the corresponding length L_{Zn} is calculated as:

$$L_{Zn} = (4n - 3)L_n, n = 2, 3, \ldots \quad (19)$$

Applying the n_{eff} calculated by the graphical method, the results for L_{Zn} are shown in Fig. 9(a), with a comparison to L_Z calculated by (2) (indicated by the diamonds). It is interesting that the part of the curves below the red dashed line overlaps with the L_Z calculated by (2). The overlapped part as redrawn
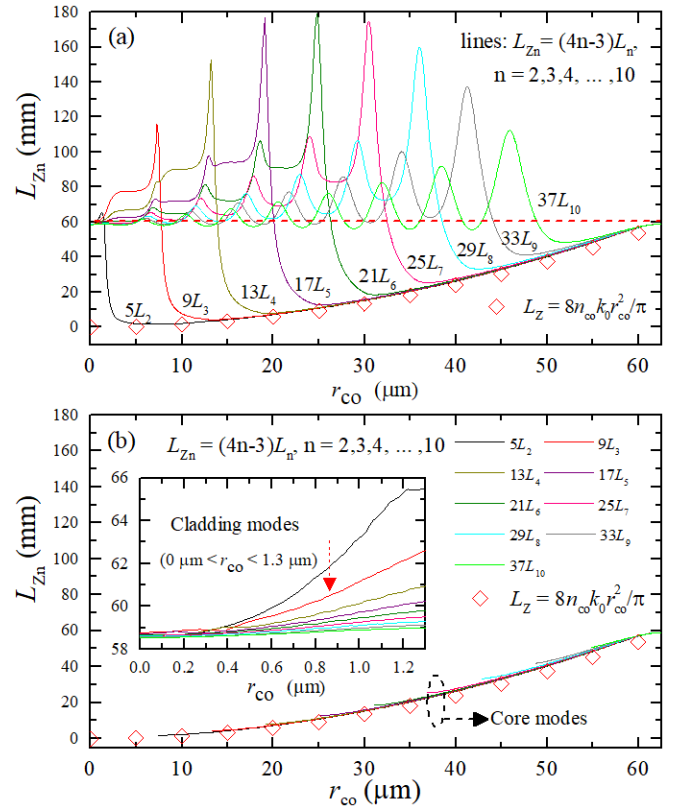
in Fig. 9(b) corresponds to the pure core modes (the range of $n_{cl} < n_{eff} < n_{co}$ in Fig. 2). The equation (2) is derived from the 2-layer model, where only the core modes are considered. The results indicate that the superposition of the pure core modes obeys the quadratic relationship between L_Z and r_{co} shown in (2) and the rule of $L_{Zn} = (4n - 3)L_n$.

On the other hand, those parts of the curves in Fig. 9(a) that deviate from the L_Z represented by (2) correspond to the cladding modes. The curves above the red dash line are separated from each other and these phenomena may be due to the mode transition and the modal re-organization shown in Fig. 2. The part of Fig. 9(a) for $r_{co} < 1.3$ μm is shown in the inset of Fig. 9(b), where the lines of L_{Zn} (n = 2, 3, …, 10) become closer as the r_{co} decreases. At the point ($r_{co} = 0$ μm), the lines converge to the value of $L_Z = (4n - 3)L_n$, the self-imaging period of NCF. The results indicate that the cladding modes in SCF with the micro/nano- core (0 μm < r_{co} < 1.3 μm) do not obey the quadratic relationship between the self-imaging period of the core modes and the core radius.

The derivation of (2) and (19) is based on an approximate expression for the n_{eff} of the core modes related to the roots of equation $J_0 = 0$ [33]. Although there were some improvements, the simulation of SMS and SNCS in most publications are still based on approximate expressions for the core modes [35], [37]. To the best of our knowledge, there has been no (approximate) analytical expression for the cladding modes in optical fiber to date. The reason may be due to the complexity of the field function (3) and the eigenvalue equation (8) of cladding modes, which is closely related to the

function Y_0 in addition to J_0 and K_0.

Although there has been no straightforward analytical expression for n_{eff} of cladding modes until now, some indications can be obtained from our simulation results. The arguments D_n ($L_Z = D_n L_n$), between the value of self-imaging period L_Z from analytical results in Fig. 8 and the L_n calculated by (18), are shown in Table I. Clearly, D_n is close to an integer 'round (D_n)', where the degree of deviation: $|D_n - round(D_n)| / D_n < 1\%$. The degree of deviation (the difference between D_n and 'round (D_n)') may be attributed to two reasons: one is the errors in the calculations of the effective index by the graphical method; the other is the phase mismatches among the excited modes, which always exist although they are quite small [36]. The 100% perfect self-imaging is impossible due to phase mismatches [36], therefore 100% integer may be also impossible.

From Table II, it is easy to obtain the expressions similar to (19), as follows:

$$L_{Zn} = (5n - 4)L_n, n = 2,3,\ldots,10, \ for \ L_Z = 5L_S \quad (20)$$
$$L_{Zn} = (6n - 5)L_n, n = 2,3,\ldots,10, \ for \ L_Z = 6L_S \quad (21)$$
$$L_{Zn} = (7n - 6)L_n, n = 2,3,\ldots,10, \ for \ L_Z = 7L_S \quad (22)$$
$$L_{Zn} = (8n - 7)L_n, n = 2,3,\ldots,10, \ for \ L_Z = 8L_S \quad (23)$$
$$L_{Zn} = (9n - 8)L_n, n = 2,3,\ldots,10, \ for \ L_Z = 9L_S \quad (24)$$
$$L_{Zn} = (10n - 9)L_n, n = 2,3,\ldots,10, \ for \ L_Z = 10L_S \quad (25)$$

We plotted together groups of lines calculated by (19)-(25) in Fig. 10. As with the group of lines converged at the position ($r_{co} = 0$ μm, $L_Z = 58.64$ mm) characterized by $(4n-3)L_n$, each of other groups also has one intersect point indicated by a violet triangle symbol. The violet triangle symbols and the violet dashed line are respectively the calculated and the exponential fitting values of the self-imaging points (radius and period) shown in the Fig. 8.

The difference between any two adjacent L_{Zn} among (19)-(25) is equal to:

$$\Delta L_{Zn} = (n - 1)L_n, n = 2,3,\ldots,10. \quad (26)$$

For n = 2, $\Delta L_{Zn} = L_2$, which is one constructive interference length of LP_{01} and LP_{02}. L_2 is longer than L_n (n > 2), deduced from (18). As shown in (19)-(25) and Table II, the self-imaging period grows as $5L_2, 6L_2, \ldots,$ and up to $11L_2$.
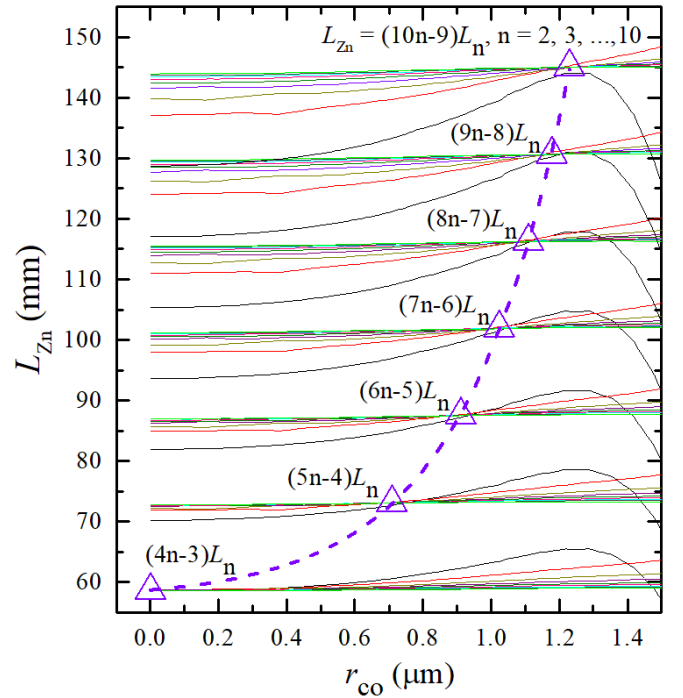

Fig. 10. The values of L_{Zn} calculated by (19)-(25). The violet triangle symbols and the violet dashed line are respectively the calculated and the exponential fitting values of self-imaging (radius and period) as same as the Fig. 8. The color of lines L_{Zn} with the same mode number 'n' is insistent with that in Fig. 9.

Therefore, it can be deduced that L_2 is the shortest distance change possible if self-imaging is to occur. Larger distance changes of the self-imaging period must be an integer multiple of L_2. The results indicate that there is no other self-imaging position between any two adjacent periods indicated by (19)-(25). For example, there is no self-imaging whose period is between $L_Z = 4L_S = 5L_2$ and $L_Z = 5L_S = 6L_2$, from (19) and (20). Therefore, the self-imaging of pure cladding modes in SSCS is discrete.

D. Experiments

To verify the above results, simulations and the experimental measurements of the transmission spectra were carried out for both the SSCS and the SNCS structures. The BPM were used in this part for its convenience and

TABLE I
THE ARGUMENTS BETWEEN THE DISCRETE SELF-IMAGING PERIODS AND THE CONSTRUCTIVE INTERFERENCE LENGTHS

r_{co} (μm)	L_Z (mm)	$D_2 = L_Z/L_2$	$D_3 = L_Z/L_3$	$D_4 = L_Z/L_4$	$D_5 = L_Z/L_5$	$D_6 = L_Z/L_6$	$D_7 = L_Z/L_7$	$D_8 = L_Z/L_8$	$D_9 = L_Z/L_9$	$D_{10} = L_Z/L_{10}$
0 (SNCS)	58.636	5.00941	8.97887	12.99934	16.98053	20.99547	25.00504	29.02002	33.04142	37.06998
0.71	73.116	6.03221	10.99033	15.9949	20.99286	25.99331	31.00182	36.0065	41.03591	46.04113
0.91	87.562	7.0293	12.98382	19.0031	24.99515	30.99758	36.99459	43.00676	49.0406	55.05314
1.02	101.953	8.04557	14.97467	22.00988	29.00472	35.99829	42.99714	50.00864	57.03445	64.05008
1.11	116.331	9.01812	16.97317	25.01795	32.99923	40.99165	48.99595	57.00807	65.01083	73.03617
1.18	130.702	10.03411	18.95392	28.0204	37.01572	45.9954	54.98189	63.98647	73.01578	82.03356
1.23	145.141	11.08954	20.92305	31.00198	41.01084	50.99464	61.00377	71.01788	81.03748	91.07236

TABLE II
THE INTEGER ARGUMENTS BETWEEN THE DISCRETE SELF-IMAGING PERIODS AND THE CONSTRUCTIVE INTERFERENCE LENGTHS

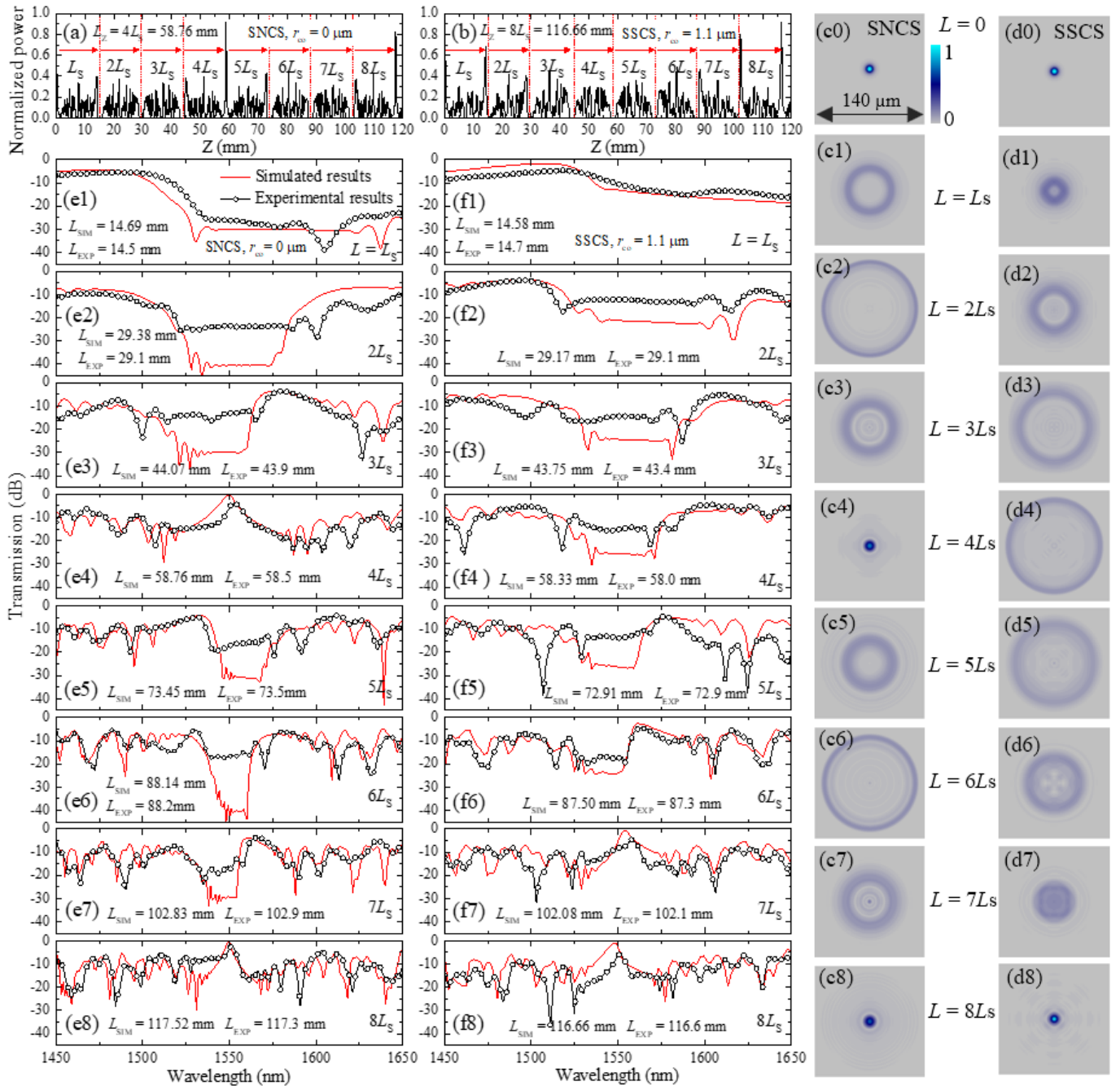| r_{co} (μm)	Round (D_2)	Round (D_3)	Round (D_4)	Round (D_5)	Round (D_6)	Round (D_7)	Round (D_8)	Round (D_9)	Round (D_{10})	Round (D_n)
0 (SNCS)	5	9	13	17	21	25	29	33	37	(4n-3)
0.71	6	11	16	21	26	31	36	41	46	(5n-4)
0.91	7	13	19	25	31	37	43	49	55	(6n-5)
1.02	8	15	22	29	36	43	50	57	64	(7n-6)
1.11	9	17	25	33	41	49	57	65	73	(8n-7)
1.18	10	19	28	37	46	55	64	73	82	(9n-8)
1.23	11	21	31	41	51	61	71	81	91	(10n-9)

Fig.11. (a) and (b) are the on-axis intensities inside the middle fiber section of SNCS (r_{co} = 0 µm) and SSCS (r_{co} = 1.1 µm). (c0)-(c8) and (d0)-(d8) show the TIPs in the middle fiber section of the SNCS and SSCS samples at the positions Z = nL_S (n = 1, 2, …, 8), where the light wavelength was set at 1550 nm. (e1)-(e8) and (f1)-(f8) show the simulated and measured transmission spectra of the samples, where the lengths of the middle fiber section are equal to the integer multiples of L_S: $1L_S$, $2L_S$, …, $8L_S$.

straightforward in the simulation of the spectrum. In the experiments, fiber type SMF28™ (from Corning) was used as the SMF, fiber type FG125LA (from Thorlabs) was used as the NCF (r_{co} = 0 µm) and fiber type SM450 (Thorlabs) was used as the SCF. The r_{co} of SM450 is about 1.1 µm, which is close to the discrete value of self-imaging radius r_{co} = 1.12 µm (in BPM results), of which the self-imaging period is L_Z = $8L_S$, as shown in Fig. 7(e). The remaining fiber parameters for the SMF28™, the FG125LA and the SM450 are same as those used in simulations, shown in section II. Figs. 11(a) and 11(b) are the on-axis intensity along the propagation distance inside the middle fiber section of the SNCS (r_{co} = 0 µm) and SSCS (r_{co} = 1.1 µm), respectively. The L_Z of the SSCS (r_{co} = 1.1 µm)

is equal to 116.66 mm ($8L_S$, L_S = 14.58 mm), which is nearly double the L_Z for the SNCS equal to 58.76 mm ($4L_S$, L_S = 14.69 mm). 16 samples were studied in two groups for the SNCS/SSCS with the lengths of the middle fiber sections (NCF/SCF) equal to the integer multiples of L_S: $1L_S$, $2L_S$, …, $8L_S$. The TIPs of the middle fiber section were also calculated for the SNCS/SSCS at the positions L = nL_S (n = 1, 2, …, 8), where the light wavelength was set at 1550 nm, as shown in the Figs. 11(c0)-11(c8) and 11(d0)-11(d8). The transmission spectra were simulated (red lines) and measured (black lines and circles) in the wavelength range from 1450 nm to 1650 nm, as shown in Figs. 11(e1)-11(e8) and 11(f1)-11(f8).

The presence of self-imaging means that the input field

profile is reproduced at periodic lengths along the middle fiber section of an OFI. For the SNCS, the reproduced input profile (single like image) can be found in Figs. 11(c4) and 11(c8) for the lengths $L = 4L_S$ and $L = 8L_S$, respectively, corresponding to the transmission peak appearing around the 1550 nm as shown in Figs. 11(e4) and 11(e8). At the other lengths $L = L_S$, $2L_S$, $3L_S$, $5L_S$, $6L_S$ and $7L_S$, a single ring-like image is observed as shown in Figs. 11(c1)-11(c3) and 11(c5)-11(c7), corresponding to the transmission notch appearing around the 1550 nm in Figs. 11(e1)-11(e3) and 11(e5)-11(e7). The transmission peak and the notch result from the constructive and destructive interference of the LP_{0n} modes. There are more dips and peaks in the transmission spectra along the second periodic interval in Figs. 11(e5)-11(e8) compared to the first periodic interval in Figs. 11(e1)-11(e4), due to more dense interference among the guided modes along the longer length of the NCF. Similarly, from the analysis of Figs. 11(b), 11(d0)-11(d8) and 11(f1)-11(f8), we can see that self-imaging appears at about $L = 8L_S$ for the SSCS ($r_{co} = 1.1$ μm). The experimental results of the transmission spectra in Figs. 11(e1)-11(e8) and 11(f1)-11(f8) match well with the simulation results.

IV. DISCUSSION

Our results show two prime characteristics of self-imaging in a SSCS structure: one is its discrete nature, the other is its exponential growth with the fiber core radius. The explicit self-imaging occurs only at the distinct sites along the propagation direction, for only a specific set of r_{co} values, hence it is discrete. The L_Z in an SSCS is an exponential function of the (discrete) values of r_{co}, while in SMS and SNCS structures the L_Z is a quadratic function of r_{co}. Nevertheless, the self-imaging of the SSCS retains some features similar to those for the SNCS. Firstly, the L_S is approximately the same in both the SNCS and SSCS structures. Secondly, the lengths for the generation of the single ring-like images or point-like images are still integer multiples of L_S. Moreover, there exists a relationship: L_Z (SSCS) = $(1+q/4)L_Z$(SNCS). It can be deduced that small changes in L_S in both SNCS and SSCS are associated with the function J_0 while the discrete growth behavior of L_Z solely in the SSCS is attributed to the additional function Y_0. The n_{eff} of the core modes, obtained by solving equation $J_0 = 0$, define the general characteristics of the self-imaging in SMS and SNCS: the relationship between L_Z and L_S ($L_Z = 4L_S$) is satisfied for all the continuous core radii. The modulation between J_0 and Y_0 in the description of the cladding modes in SSCS not only reflects the observed modal reorganization behavior, but also results in a more complex mode superposition compared to that of core modes.

The discrete self-imaging effect in an SSCS can be regarded as the first discrete self-imaging phenomenon found in the multimode waveguide. As a counterpart in one-dimensional waveguide arrays, the discrete Talbot self-imaging effect was first found in 2005 by Robert Iwanow *et al.*, who stated that the self-imaging of the input field pattern is only possible for a specific set of periodicities [44]. The waveguide arrays consisted of a large number (infinite in principle) of periodic evanescently coupled single-mode

channel waveguides, which is a form of discrete system where the field evolution equation is effectively discretized (discrete diffraction) and is capable of nonlinear effects and even the discrete optical solitons [45], [46]. Analogously, the discrete self-imaging effect in SSCS indicates that the SCF may be also a discrete multimode physical system. The SCF with pure cladding modes may be a valuable platform for studying multimode nonlinear fiber optics. It is also expected that the multimode solitons, which so far have been only experimentally observed in the graded-index multimode fiber [2], could be achieved in an SCF.

The unique light field of multiple cladding-type modes in the SCF, distinct from that of multiple core-type modes in the commonly used MMF and NCF, can be further explored in many applications. For example, compared to the Bessel beams generated by NCF or MMF and characterized by the function J_0 [4], [5], the pure cladding modes in a SCF can be used to generate a new kind of Bessel beams characterized by the combinations of J_0 and Y_0. Bessel beams based on a truncation of Y_0 having higher energy over a longer range than that of J_0 Bessel beams were theoretically predicted in [47]. Indeed, the micro/nano- core in SCFs can strongly modify the on-axis intensity, which is critically important to the performance of Bessel beams in the optical manipulation [48], [49]. Therefore the Y_0 modulated J_0 Bessel beams generated with SCFs may offer a better performance in optical manipulation applications.

V. CONCLUSION

The effective refractive index of both the core-type and cladding-type modes LP_{0n} in three-layer step-index optical fibers as a function of core radius, was calculated independently by the graphical method and the BPM. The cladding modes show a kind of modal reorganization characteristics, indicating a different behavior with that of core modes. The self-imaging of cladding modes in an SSCS was analytically and numerically calculated and confirmed by interference spectrum experiments for the first time. The self-imaging in the SSCS shows the discrete nature and the behavior of exponential growth with the core radius of middle fiber section. The analysis of the constructive interference of adjacent guided modes shows that the self-imaging must be discrete since the change in distance of the self-imaging period must be integer multiple of L_2 (the constructive interference length of LP_{01} and LP_{02}). The discrete nature and exponential growth behavior found by our work indicates that the propagation properties of cladding modes in an SCF are distinct from that of the core modes in the commonly used NCF and MMF. The SCF may be a discrete multimode physical system, which deserves further study in the context of nonlinear multimode fiber optics. The distinctive physical characteristics of the self-imaging in the SSCS may provide new insights and rules in the design of the multi-mode interference devices such as optical couplers, optical modulators, multimode fiber lasers and space-division multiplexing systems.

REFERENCES

[1] D. Richardson, J. Fini, and L. Nelson, "Space-division multiplexing in optical fibres," Nature Photonics, vol. 7, no. 5, p. 354, 2013.

[2] W. H. Renninger and F. W. Wise, "Optical solitons in graded-index multimode fibres," Nature communications, vol. 4, p. 1719, 2013.

[3] M. Plöschner, T. Tyc, and T. Čižmár, "Seeing through chaos in multi- mode fibres," Nature Photonics, vol. 9, no. 8, p. 529, 2015.

[4] Y. Zhang, X. Tang, Y. Zhang, Z. Liu, E. Zhao, X. Yang, J. Zhang, J. Yang, and L. Yuan, "Multiple particles 3-d trap based on all-fiber bessel optical probe," Journal of Lightwave Technology, vol. 35, no. 18, pp. 3849–3853, 2017.

[5] S. R. Lee, J. Kim, S. Lee, Y. Jung, J. K. Kim, and K. Oh, "All-silica fiber bessel-like beam generator and its applications in longitudinal optical trapping and transport of multiple dielectric particles," Optics express, vol. 18, no. 24, pp. 25299–25305, 2010.

[6] M. N. Zervas and C. A. Codemard, "High power fiber lasers: a review," IEEE Journal of selected topics in Quantum Electronics, vol. 20, no. 5, pp. 219–241, 2014.

[7] H. Chen, C. Jin, B. Huang, N. Fontaine, R. Ryf, K. Shang, N. Grégoire, S. Morency, R.-J. Essiambre, G. Li et al., "Integrated cladding-pumped multicore few-mode erbium-doped fibre amplifier for space-division-multiplexed communications," Nature Photonics, vol. 10, no. 8, p. 529, 2016.

[8] L. G. Wright, Z. M. Ziegler, P. M. Lushnikov, Z. Zhu, M. A. Eftekhar, D. N. Christodoulides, and F. W. Wise, "Multimode nonlinear fiber optics: Massively parallel numerical solver, tutorial, and outlook," IEEE Journal of Selected Topics in Quantum Electronics, vol. 24, no. 3, pp. 1–16, 2018.

[9] J. Carpenter, B. J. Eggleton, and J. Schröder, "Observation of eisenbud–wigner–smith states as principal modes in multimode fibre," Nature Photonics, vol. 9, no. 11, p. 751, 2015.

[10] K. Krupa, A. Tonello, B. M. Shalaby, M. Fabert, A. Barthélémy, G. Millot, S. Wabnitz, and V. Couderc, "Spatial beam self-cleaning in multimode fibres," Nature Photonics, vol. 11, no. 4, p. 237, 2017.

[11] O. V. Ivanov, S. A. Nikitov, and Y. V. Gulyaev, "Cladding modes of optical fibers: properties and applications," Physics-Uspekhi, vol. 49, no. 2, pp. 167–191, 2006.

[12] C. Caucheteur, T. Guo, F. Liu, B.-O. Guan, and J. Albert, "Ultrasensitive plasmonic sensing in air using optical fibre spectral combs," Nature communications, vol. 7, p. 13371, 2016.

[13] Y. Li and T. Erdogan, "Cladding-mode assisted fiber-to-fiber and fiber- to-free-space coupling," Optics communications, vol. 183, no. 5-6, pp. 377–388, 2000.

[14] C. Tsao, Optical fibre waveguide analysis. Oxford University Press, 1992.

[15] M. Z. Alam and J. Albert, "Selective excitation of radially and azimuthally polarized optical fiber cladding modes," Journal of Lightwave Technology, vol. 31, no. 19, pp. 3167–3175, 2013.

[16] R. Guyard, D. Leduc, C. Lupi, and Y. Lecieux, "Critical cladding radius for hybrid cladding modes," Optics & Laser Technology, vol. 101, pp. 116–126, 2018.

[17] A. W. Snyder and J. Love, Optical waveguide theory. Springer Science & Business Media, 2012.

[18] L. C. Bobb, P. Shankar, and H. D. Krumboltz, "Bending effects in biconically tapered single-mode fibers," Journal of lightwave technology, vol. 8, no. 7, pp. 1084–1090, 1990.

[19] Q. Wu, Y. Semenova, P. Wang, and G. Farrell, "A comprehensive analysis verified by experiment of a refractometer based on an smf28– small-core singlemode fiber (scsmf)–smf28 fiber structure," Journal of Optics, vol. 13, no. 12, p. 125401, 2011.

[20] L. Tong, F. Zi, X. Guo, and J. Lou, "Optical microfibers and nanofibers: A tutorial," Optics Communications, vol. 285, no. 23, pp. 4641–4647, 2012.

[21] F. Xu, Z.-x. Wu, and Y.-q. Lu, "Nonlinear optics in optical-fiber nanowires and their applications," Progress in Quantum Electronics, vol. 55, pp. 35–51, 2017.

[22] L. Tong, R. R. Gattass, J. B. Ashcom, S. He, J. Lou, M. Shen, I. Maxwell, and E. Mazur, "Subwavelength-diameter silica wires for low-loss optical wave guiding," Nature, vol. 426, no. 6968, p. 816, 2003.

[23] D. Marcuse, Theory of Dielectric Optical Waveguides. Academic press Inc., 1991.

[24] J. A. Buck, Fundamentals of optical fibers. John Wiley & Sons, 2004.

[25] I. Del Villar, I. R. Matías, F. J. Arregui, and P. Lalanne, "Optimization of sensitivity in long period fiber gratings with overlay deposition," Optics Express, vol. 13, no. 1, pp. 56–69, 2005.

[26] A. B. Socorro, I. Del Villar, J. M. Corres, F. J. Arregui, and I. R. Matias, "Mode transition in complex refractive index coated single-mode–multimode–single-mode structure," Optics express, vol. 21, no. 10, pp. 12668–12682, 2013.

[27] D. Marcuse, "Mode conversion in optical fibers with monotonically increasing core radius," Journal of lightwave technology, vol. 5, no. 1, pp. 125–133, 1987.

[28] J. Kerttula, V. Filippov, V. Ustimchik, Y. Chamorovskiy, and O. G. Okhotnikov, "Mode evolution in long tapered fibers with high tapering ratio," Optics Express, vol. 20, no. 23, pp. 25461–25470, 2012.

[29] Y. Jung, G. Brambilla, and D. J. Richardson, "Broadband single-mode operation of standard optical fibers by using a sub-wavelength optical wire filter," Optics Express, vol. 16, no. 19, pp. 14661–14667, 2008.

[30] X. Jiang, L. Shao, S.-X. Zhang, X. Yi, J. Wiersig, L. Wang, Q. Gong, M. Lončar, L. Yang, and Y.-F. Xiao, "Chaos-assisted broadband momentum transformation in optical microresonators," Science, vol. 358, no. 6361, pp. 344–347, 2017.

[31] L. Tong, J. Lou, and E. Mazur, "Single-mode guiding properties of subwavelength-diameter silica and silicon wire waveguides," Optics Express, vol. 12, no. 6, pp. 1025–1035, 2004.

[32] L. B. Soldano and E. C. Pennings, "Optical multi-mode interference devices based on self-imaging: principles and applications," Journal of lightwave technology, vol. 13, no. 4, pp. 615–627, 1995.

[33] W. S. Mohammed, A. Mehta, and E. G. Johnson, "Wavelength tunable fiber lens based on multimode interference," Journal of Lightwave Technology, vol. 22, no. 2, p. 469, 2004.

[34] Q. Wang, G. Farrell, and W. Yan, "Investigation on single-mode–multimode–single-mode fiber structure," Journal of Lightwave Technology, vol. 26, no. 5, pp. 512–519, 2008.

[35] W. Xu, J. Shi, X. Yang, D. Xu, F. Rong, J. Zhao, and J. Yao, "Improved numerical calculation of the single-mode-no-core-single-mode fiber structure using the fields far from cutoff approximation," Sensors, vol. 17, no. 10, p. 2240, 2017.

[36] X. Zhu, A. Schülzgen, H. Li, L. Li, L. Han, J. Moloney, and N. Peyghambarian, "Detailed investigation of self-imaging in large core multimode optica l fibers for application in fiber lasers and amplifiers," Optics Express, vol. 16, no. 21, pp. 16632–16645, 2008.

[37] J. Zheng, J. Li, T. Ning, L. Pei, S. Jian, and Y. Wen, "Improved self-imaging for multi-mode optical fiber involving cladding refractive index," Optics Communications, vol. 311, pp. 350–353, 2013.

[38] K. Hamamoto and H. Jiang, "Active mmi devices: concept, proof, and recent progress," Journal of Physics D: Applied Physics, vol. 48, no. 38, p. 383001, 2015.

[39] N. Li, M. Liu, X. Gao, L. Zhang, Z. Jia, Y. Feng, Y. Ohishi, G. Qin, and W. Qin, "All-fiber widely tunable mode-locked thulium-doped laser using a curvature multimode interference filter," Laser Physics Letters, vol. 13, no. 7, p. 075103, 2016.

[40] X. Zhao, G. Bai, Y. Zheng, X. Chen, Y. Yang, K. Liu, C. Zhao, Y. Qi, B. He, J. Zhou et al., "Mode suppression employing periodical large-small-core (plsc) filter in strongly pumped large mode area fiber amplifier," Journal of Optics, vol. 19, no. 6, p. 065801, 2017.

[41] K. Krupa, A. Tonello, A. Barthélémy, V. Couderc, B. M. Shalaby, A. Bendahmane, G. Millot, and S. Wabnitz, "Observation of geometric parametric instability induced by the periodic spatial self-imaging of multimode waves," Physical review letters, vol. 116, no. 18, p. 183901, 2016.

[42] L. G. Wright, S. Wabnitz, D. N. Christodoulides, and F. W. Wise, "Ultrabroadband dispersive radiation by spatiotemporal oscillation of multimode waves," Physical review letters, vol. 115, no. 22, p. 223902, 2015.

[43] M. Michel. "Propagation in doubly clad single-mode fibers." IEEE Transactions on Microwave Theory and Techniques, vol. 30, no. 4, p. 381-388, 1982.

[44] R. Iwanow, D. A. May-Arrioja, D. N. Christodoulides, G. I. Stegeman, Y. Min, and W. Sohler, "Discrete talbot effect in waveguide arrays," Physical review letters, vol. 95, no. 5, p. 053902, 2005.

[45] I. L. Garanovich, S. Longhi, A. A. Sukhorukov, and Y. S. Kivshar, "Light propagation and localization in modulated photonic lattices and waveguides," Physics Reports, vol. 518, no. 1-2, pp. 1–79, 2012.

[46] F. Lederer, G. I. Stegeman, D. N. Christodoulides, G. Assanto, M. Segev, and Y. Silberberg, "Discrete solitons in optics," Physics Reports, vol. 463, no. 1-3, pp. 1–126, 2008.

[47] L. Vicari, "Truncation of non-diffracting beams," Optics communications, vol. 70, no. 4, pp. 263–266, 1989.

[48] D. McGloin and K. Dholakia, "Bessel beams: diffraction in a new light," Contemporary Physics, vol. 46, no. 1, pp. 15–28, 2005.

[49] T. Čižmár, V. Kollárová, Z. Bouchal, and P. Zemánek, "Sub-micron particle organization by self-imaging of non-diffracting beams," New Journal of Physics, vol. 8, no. 3, p. 43, 2006.